Near-Inertial Wave Energetics Modulated by Background Flows in a Global Model Simulation

KESHAV J. RAJA,[a] MAARTEN C. BUIJSMAN,[a] JAY F. SHRIVER,[b] BRIAN K. ARBIC,[c] AND OLADEJI SIYANBOLA[a]

[a] *School of Ocean Science and Engineering, University of Southern Mississippi, Stennis Space Center, Mississippi*
[b] *Ocean Dynamics and Prediction Branch, Naval Research Laboratory, Stennis Space Center, Mississippi*
[c] *Department of Earth and Environmental Sciences, University of Michigan, Ann Arbor, Michigan*

(Manuscript received 15 June 2021, in final form 23 December 2021)

ABSTRACT: We study the generation, propagation, and dissipation of wind-generated near-inertial waves (NIWs) in a global 1/25° Hybrid Coordinate Ocean Model (HYCOM) simulation with realistic atmospheric forcing and background circulation during 30 days in May–June 2019. The time-mean near-inertial wind power input and depth-integrated energy balance terms are computed for the total fields and the fields decomposed into vertical modes to differentiate between the radiative and (locally) dissipative components of NIW energy. Only 30.3% of the near-inertial wind input projects onto the first five modes, whereas the sum of the NIW energy in the first five modes adds up to 58% of the total NIW energy. Almost all of the depth-integrated NIW horizontal energy flux projects on the first five modes. The global distribution of dissipation and decay distances of NIW modes confirm that lower latitudes are a sink for NIW energy generated at higher latitudes. The locally dissipated fraction of NIW energy q_{local} is found to be uniform throughout the global ocean, with a global mean value of 0.79. The horizontal NIW fluxes diverge from areas with cyclonic vorticity and converge in areas with anticyclonic vorticity; that is, anticyclonic eddies are a sink for NIW energy fluxes—in particular, for higher modes. Most of the residual energy that does not project onto modes propagates downward in anticyclonic eddies. The global near-inertial wind power input is 0.21 TW for the 30 days, of which only 19% is transmitted below 500-m depth.

KEYWORDS: Inertia–gravity waves; Internal waves; Ocean models

1. Introduction

Diapycnal mixing in the ocean interior plays an important role in supporting the upwelling part of the meridional overturning circulation (MOC). It is estimated that about 2 ± 0.6 TW (1 TW = 10^{12} W) of power is required to maintain the MOC through ocean mixing (Munk and Wunsch 1998; Kunze 2017). Internal wave breaking is the dominant source of diapycnal mixing in most of the ocean interior (Munk and Wunsch 1998; MacKinnon et al. 2017). Deep ocean internal waves have primarily 3 sources: internal tides generated by tide–topography interaction at 1 TW of power (Egbert and Ray 2001; MacKinnon et al. 2017; Vic et al. 2019; de Lavergne et al. 2019; Buijsman et al. 2020), wind-generated near-inertial motions at 0.16–0.50 TW of power (Alford 2003; Furuichi et al. 2008; Flexas et al. 2019; Alford 2020b), and topography-generated internal lee waves at 0.06–0.51 TW of power (Scott et al. 2011; Nikurashin and Ferrari 2011; Trossman et al. 2013; Shakespeare 2020). The contribution from wind-generated near-inertial waves (NIWs) to internal wave power input has a large uncertainty. We still do not fully understand the details of NIW dynamics and how they interact with other processes in the ocean. A part of the uncertainty is also associated with the spatial and temporal resolution of global wind products, in particular at high latitudes (Kunze 2017; Jiang et al. 2005; Rimac et al. 2013). Thus, the understanding of NIW energy budget and how different near-surface processes interact with NIWs are essential to accurately estimate the role of NIWs in driving deep ocean mixing.

The wind power input to surface near-inertial motions has been estimated by numerous studies. Early studies have all used the slab mixed layer model of Pollard and Millard (1970) and computed the global annual-mean wind power input to surface near-inertial motions ranging from 0.3 to 1.1 TW (Alford 2001; Watanabe and Hibiya 2002; Alford 2003) depending on the spatiotemporal resolution of the wind product used (Jiang et al. 2005; Rimac et al. 2013). The slab models, however, are prone to overestimate the wind work as they do not account for the energy loss due to vertical shear instability, mixed layer deepening or the radiation into the ocean interior (Plueddemann and Farrar 2006; Furuichi et al. 2008). Alford (2020b) reviews the various definitions of near-inertial wind work using slab models. He examines the mixed layer potential energy increase and compares it with the estimate from Argo and ERA-Interim heat flux climatology. He finds that more than 50% of near-inertial surface wind power input is lost to turbulence in the upper layers and is not available to propagating NIWs.

With regard to global ocean simulations, Furuichi et al. (2008) used a full three-dimensional primitive equation model for a global ocean with 1/7° resolution (in longitude) forced by 6-hourly wind stress and estimated the annual-mean surface near-inertial wind power input to be 0.4 TW. Recently, Flexas et al. (2019) performed a high-resolution (1/48°) realistic global ocean simulation with tidal forcing to estimate wind work on the oceans. They used 6-hourly winds

---

Corresponding author: Keshav J. Raja, keshav.raja@usm.edu

DOI: 10.1175/JPO-D-21-0130.1

with 0.14° resolution and found 0.16 TW of annual mean surface near-inertial wind power input. They concluded that wind variability on time scales less than 6 h and spatial scales less than 15 km is crucial to accurately represent the wind power input in ocean models.

The wind-generated near-inertial motions in the surface mixed layer have lateral variations due to vorticity gradients leading to convergences and divergences that cause vertical motions at the base of the mixed layer. These vertical motions generate NIWs in the ocean interior (Gill 1984; D'Asaro et al. 1995). Gill (1984) developed a modal formalism to describe these motions in the ocean interior, which take the form of standing vertical oscillations, called normal modes. The horizontal propagation of NIWs from their generation sites to far away locations can be better understood using the method of vertical normal modes (Simmons and Alford 2012; Kelly 2019). Observational data from the Ocean Storms Experiment (D'Asaro et al. 1995) and moorings (Alford 2003) show that NIW energy can radiate long distances equatorward away from its generation site as mode 1 and mode 2 waves before dissipating. Simmons and Alford (2012) used a 1/8° fully eddying isopycnal global ocean model to study long range propagation of NIWs. Their model was forced by 6-hourly winds. They found that as much as 3%–16% of NIW energy radiates out of its generation sites and equatorward as low-mode internal gravity waves. Since Alford et al. (2012), there has been little effort to understand the radiative versus (locally) dissipative partitioning of NIW energy in global ocean simulations.

The transfer of wind power from the ocean surface to the interior is facilitated by several processes. The horizontal scales of surface near-inertial motions can be of the order of 1000 km corresponding to the wind event that generated them. Since the vertical group velocity of near-inertial waves is proportional to their horizontal wavenumber, these waves cannot propagate rapidly in the vertical direction unless their horizontal scales are reduced (Gill 1984). One of the processes that can reduce the horizontal scales of near-inertial motions is the β-dispersion effect, whereby near-inertial motions are progressively dephased as a result of the planetary vorticity gradient, resulting in smaller horizontal wavelengths and faster vertical propagation. This process has been observed by D'Asaro et al. (1995).

Another process that has been hypothesized to shift the local inertial frequency and modulate the propagation of NIWs is the refraction of waves by the mesoscale vorticity in the ocean (Kunze 1985; Young and Jelloul 1997; Lee and Niiler 1998; Asselin and Young 2020). An effective Coriolis parameter can be defined by $f_{\text{eff}} = f + \zeta/2$, where f is the Coriolis parameter and ζ is the relative vorticity (Mooers 1975). This frequency shift can lead to the trapping of near-inertial energy in regions of negative relative vorticity (Lee and Niiler 1998). Since the gradients of relative vorticity are much larger than the β effect, the frequency shift to f_{eff} might be a stronger effect in accelerating vertical propagation of near-inertial energy locally. Rimac (2014) examined the influence of relative vorticity in NIW energy transmission using two global ocean simulations with horizontal resolutions of 0.1° (resolving most of the mesoscale eddies) and 0.4° (hardly resolving any eddies) and found enhanced NIW kinetic energy (KE) in the interior of the ocean in the simulation with eddies. However, Rimac (2014) did not consider a detailed energy analysis, nor did she correlate the energy of near-inertial modes with vorticity.

In this paper, we study the depth-integrated energetics of NIWs in realistically forced global ocean simulations with the Hybrid Coordinate Ocean Model (HYCOM). We determine what fraction of total near-inertial wind input, energy, and dissipation can be attributed to the resolved vertical modes. We examine the global spatial patterns of the total, modal, and residual NIW energy terms and study how these energy terms are modulated by the background vorticity. Such comprehensive depth-integrated NIW global energy balance has not yet been done. Our simulations have a horizontal resolution of 1/25° and a 3-hourly wind forcing, which is an improvement over the global ocean simulations mentioned above. Previous model studies either have a coarser resolution or lower-frequency wind forcing, or both. Moreover, the advantage of using the isopycnal coordinate HYCOM model, instead of fixed vertical coordinates, is that the effect of numerical diffusion is minimized (Halliwell 2004). This is beneficial for studying the long-range propagation of NIWs. HYCOM has been extensively validated and optimized for surface and internal tidal waves (Arbic et al. 2012; Ansong et al. 2015; Arbic et al. 2018; Buijsman et al. 2016, 2020). However, we do not yet know how much wind energy is transferred to near-inertial gravity waves, how they propagate, and where these waves dissipate in global HYCOM simulations.

In the next section, we describe the HYCOM model configuration and our analysis methods. In section 3, we present the results of the depth-integrated near-inertial energy budget of the undecomposed fields and the fields decomposed into vertical modes. We discuss global maps of the near-inertial wind input, the NIW energy, the horizontal energy fluxes, and the dissipation. Moreover, we analyze the influence of background vorticity on the NIW energetics of the total, modal, and residual fields. We also examine the vertical transmission of NIW energy. We discuss the implication of our results and examine the limitations of our methods in section 4. Our most relevant findings are summarized in the conclusions in section 5.

2. Methods

a. HYCOM

We use the HYCOM (Metzger et al. 2014), which is the operational forecast model of the U.S. Navy. The model uses a hybrid vertical coordinate system, which is isopycnal in the deep ocean and employs z coordinates to resolve the surface mixed layer. The model coordinates transition to terrain following in shallow water. The simulation runs on a tripolar grid at 1/25° horizontal resolution and 41 layers in the vertical direction (approximately one-half of the levels are above 250 m, most of them 8 m apart in the open ocean). A K-profile parameterization is used as the subgrid-scale mixing model in the simulation. We analyze a forward (non–data assimilative) simulation without tidal forcing, also referred to as EXPT 19.2 in HYCOM terminology. The simulation has realistic atmospheric forcing from the Navy Global Environmental Model (NAVGEM) (Hogan et al. 2014) with 60 atmospheric levels over a height of 19 km, 0.17° horizontal resolution, and 3-hourly wind forcing. The output variables are stored every hour. In this paper, we diagnose NIW energetics from 20 May to 19 June 2019 (30 days), which coincides with the cruises in the North Atlantic Ocean as part of the Near Inertial Shear and Kinetic Energy in the North Atlantic experiment (NISKINe). In the appendix, we also examine a simulation with astronomical tidal forcing, EXPT 19.0, which is a twin of EXPT 19.2. EXPT 19.0 is forced with the M_2, S_2, K_1, O_1, and N_2 tidal constituents (Buijsman et al. 2020). In the simulation with tides, the parametric subharmonic instability (PSI) of internal tides generates near-inertial motions (Hazewinkel and Winters 2011; Ansong et al. 2018), which we do not account for in our NIW energy equations. Additionally, the nonstationary diurnal internal tides cannot be fully removed near the critical latitudes in the simulation with tides. Hence, we choose to use the simulation without tides for our analysis of NIW energetics. Both EXPT 19.0 and 19.2 are forward runs initiated from EXPT 21.6, a global HYCOM simulation with data assimilation (DA) and tides. The tidal forcing and DA were turned off on 1 April 2019 (50 days before the analysis period), providing enough time for the internal tides and disturbances related to DA to dissipate.

b. NIW energetics

The near-inertial fields are obtained from the model output after removing any remaining stationary tides using a harmonic analysis and by applying a bandpass filter with frequency limits $0.8f$–1/13.21 h equatorward of 56° and $0.8f$–$1.2f$ poleward of 56°. This filter is applied to both our simulations with and without tides. It is designed in such a way that semidiurnal internal tides that are generated poleward of 56° and propagate equatorward are removed. Moreover, with this filter, we capture NIWs that have propagated a large distance from their generation sites.

We use the filtered near-inertial fields to calculate the time-mean, depth-integrated near-inertial energy equation (Alford and Zhao 2007a; Zhai et al. 2009):

$$\overline{W} = \overline{\frac{\partial E}{\partial t}} + \nabla\cdot(\overline{\mathbf{F}_H} + \overline{\mathbf{F}_a}) + \overline{D}, \tag{1}$$

where the overbar indicates time-average over 30 days, W is the near-inertial surface wind power input, E is the depth-integrated near-inertial energy, $\mathbf{F}_H$ is the depth-integrated horizontal NIW energy flux, $\mathbf{F}_a$ is the energy flux due to the self-advection of NIW energy and D is the depth-integrated internal wave dissipation, considered to be a residual term.

The wind power input to surface near-inertial motions is calculated as $W = \boldsymbol{\tau}\cdot\mathbf{u}(z=0)$, where $\boldsymbol{\tau}$ is the near-inertial surface wind stress and $\mathbf{u}(z=0)$ is the horizontal baroclinic near-inertial velocity vector at the surface. The total wind stress is computed during the simulation. The near-inertial surface wind stress can inject power into mixed layer inertial motions that project on both baroclinic and barotropic modes. However, we verify that the wind input to barotropic near-inertial motions is negligible relative to the wind input to baroclinic near-inertial motions.

The depth-integrated near-inertial energy E is the sum of the depth-integrated kinetic energy

$$\mathrm{KE} = \frac{1}{2}\rho_0\int_{-H}^{0}|\mathbf{u}|^2\,dz, \tag{2}$$

and the depth-integrated available potential energy (Kang and Fringer 2010)

$$\mathrm{APE} = \frac{1}{2}\rho_0\int_{-H}^{0}\frac{b^2}{N^2}\,dz, \tag{3}$$

where H is the seafloor depth, $b = g\rho/\rho_0$ is the near-inertial buoyancy, and N is the buoyancy frequency.

We calculate the depth integrated NIW energy fluxes as

$$\mathbf{F}_H = \int_{-H}^{0}p\mathbf{u}\,dz, \tag{4}$$

where the near-inertial pressure perturbations p are computed using the density anomaly ρ, as in Nash et al. (2005). The depth-integrated energy flux due to self-advection of NIW energy is calculated as

$$\mathbf{F}_a = \int_{-H}^{0}\mathbf{u}\left(\frac{1}{2}\rho_0|\mathbf{u}|^2 + \frac{1}{2}\rho_0\frac{b^2}{N^2}\right)dz. \tag{5}$$

We find that global area-averaged variance of $\overline{\partial E/\partial t}$ and $\overline{\nabla\cdot\mathbf{F}_a}$ are negligible (<1%) as compared with the variance of $\overline{\nabla\cdot\mathbf{F}_H}$. Therefore, we do not present maps of $\overline{\partial E/\partial t}$ and $\overline{\mathbf{F}_a}$ in this paper. The residual term D in Eq. (1) is dominated by viscous dissipation of NIW energy and energy lost to wave drag (Buijsman et al. 2016) but also includes energy transfers between frequency bands through wave–wave and wave–mean flow interactions, topographic scattering, and other nonlinear processes (Polzin and Lvov 2011; Le Boyer and Alford 2021). We assume that these processes lead to motions that dissipate locally.

The three-dimensional (3D) HYCOM fields are also decomposed into vertical normal modes and the NIW energy balance for these modes is computed. We largely follow the modal decomposition presented in Kelly (2016) and Buijsman et al. (2020). However, in the present analysis we decompose the baroclinic fields into vertical normal modes in the HYCOM layer space itself (as opposed to Buijsman et al. (2020), where the fields are interpolated onto an equidistant z grid). The horizontal resolution of our model (1/25°; 4 km near the equator) allows the first five vertical modes to be resolved in most of the ocean (Buijsman et al. 2020).

The hydrostatic Sturm-Liouville equation is solved for non-equidistant layers following Singh and Bhadauria (2009), using 30-day mean profiles of buoyancy frequency in each horizontal grid cell. The Sturm-Liouville equation reads

$$\frac{\partial^2 \mathcal{W}_n(z)}{\partial z^2} + \frac{N^2(z)}{c_n^2}\mathcal{W}_n(z) = 0, \qquad (6)$$

where $\mathcal{W}_n(z)$ is the eigenfunction of mode n, z is the vertical coordinate, and $N(z)$ is the buoyancy frequency. The eigenfunctions obey a rigid lid boundary condition at surface and bottom ($\mathcal{W}_n = 0$ at $z = 0, -H$). The eigenspeed $c_n = \sqrt{\omega^2 - f^2}/k_n$, where ω is the wave frequency and k_n is the horizontal wavenumber of mode n. The horizontal velocity eigenfunction is computed as

$$\mathcal{U}_n(z) = \frac{\partial \mathcal{W}_n(z)}{\partial z}. \qquad (7)$$

The horizontal velocity eigenfunctions $\mathcal{U}_n$ are projected onto the vertical profiles of the horizontal baroclinic velocities and perturbation pressures at every time step to yield the modal amplitudes in each horizontal grid cell; for example, for horizontal velocity,

$$\hat{u}_n(t) = \frac{1}{H}\int_{-H}^{0} \mathcal{U}_n(z)u(z,t)\,dz, \qquad (8)$$

where $\hat{u}_n$ is the modal amplitude of the nth mode along the x axis.

After obtaining the modal amplitudes from the unfiltered fields, we use a harmonic analysis and a bandpass filter as explained earlier to remove any remaining internal tides and to isolate the near-inertial field. We then compute the terms in the depth-integrated and time-averaged modal near-inertial energy equation

$$\overline{W_n} = \overline{\frac{\partial E_n}{\partial t}} + \nabla \cdot \overline{\mathbf{F}_n} + \overline{D_n}. \qquad (9)$$

The modal wind power input is given by $W_n = \boldsymbol{\tau} \cdot \mathbf{u}_n(z = 0)$, where $\mathbf{u}_n(z = 0) = \mathcal{U}_n(z = 0) \cdot \hat{u}_n$ is the nth mode near-inertial velocity vector at the surface of the ocean (Furuichi et al. 2008). The modal energy E_n is computed following Buijsman et al. (2020) as

$$E_n = \frac{1}{2}\rho_0 H\left[|\hat{u}_n|^2 + \frac{|\hat{p}_n|^2}{(\rho_0 c_n)^2}\right]. \qquad (10)$$

The depth-integrated modal horizontal energy flux is given by $\mathbf{F}_n = H\hat{\mathbf{u}}_n\hat{p}_n$ where $\hat{\mathbf{u}}_n$ and $\hat{p}_n$ are the modal amplitudes of the horizontal velocity vector and perturbation pressure. The residual term D_n includes dissipation of near-inertial modal energy, and also any mode–mode or mode–mean flow energy transfers, which we do not explicitly calculate in our analysis. Note that the time-averaged tendency term $\overline{\partial E_n/\partial t}$ is close to zero and is ignored in our analysis. In the remainder of the paper, we will drop the overbars when discussing the time-averaged terms of Eqs. (1) and (9).

The near-inertial energy propagates at the group velocity. We can calculate the horizontal group velocity of each mode following Alford and Zhao (2007b) as

$$c_{g,n} = \frac{|\mathbf{F}_n|}{E_n}. \qquad (11)$$

We note that the group speed of a vertical mode from linear theory, $c_{g,n} = (\omega^2 - f^2)/(k_n\omega)$, is difficult to compute because it is impractical to determine the generation frequency ω of each remote NIW. The $c_{g,n}$ at a location, calculated from Eq. (11) is, in a sense, an average group velocity of all the wave groups (with different ω) present at the location.

Furthermore, we estimate the time scale for the decay of a propagating NIW mode by $T_{d,n} = E_n/D_n$. Hence, the decay length scale for each near-inertial mode is

$$L_d = c_{g,n}T_{d,n}. \qquad (12)$$

The zonally averaged L_d helps us to identify the presence of remotely generated NIWs and quantify the distance traveled by them at each latitude.

3. Results

a. Near-inertial wind power input

The wind stress acting on the ocean surface excites motions at the base of the mixed layer that transfer the wind power to NIWs. The 30-day mean, near-inertial wind power input to the total (undecomposed) fields, to modes 1–5, and to the sum of five modes are shown in Fig. 1. The wind input to the undecomposed fields is enhanced in regions of high mesoscale energy such as in the Southern Ocean and western boundary current regions. Regions of high mesoscale activity have high surface wind stress and extract more energy from the wind. The wind power input in the Arabian Sea (~20°N, 430°E) is enhanced due to the Tropical Cyclone Vayu during 10–17 June 2019 (Mishra et al. 2021). The wind input to the sum of modes 1–5 in Fig. 1b is also enhanced in regions of high mesoscale activities but is smaller than the wind input to the undecomposed fields. The wind input to modes 1–5 in Figs. 1c–g has an almost identical distribution. Most of the wind input in these modes are in the Southern Ocean (south of 30°S). Mode 2 has the largest wind input in areas south of Africa and west of South America, while modes 3–5 have wind input throughout the Southern Ocean. The regions of the western boundary currents have most of the wind input going to modes 3–5, while in the Sea of Japan, modes 1–2 dominate.

The zonal mean wind power input to modes and the undecomposed fields, as well as other energy terms, are presented in Fig. 2a. In the following sections, we keep referencing to this figure. The wind power input in the Southern Hemisphere is much higher than in Northern Hemisphere for May–June 2019. The zonal mean wind input has distinct peaks near latitudes 50°S, 38°S, and 39°N. These correspond to regions of high mesoscale energy in the Southern Ocean and western boundary currents.

The globally integrated time-mean wind power input to the undecomposed fields and the modes is shown in Fig. 1h. The global mean surface near-inertial wind power input in our simulation for May–June 2019 is 0.21 TW. This is in agreement with the 0.24 TW value obtained by Simmons and Alford (2012) for the month of May-June in their global simulation. The wind power input to the first 4 modes is almost equally distributed. The sum of wind power contributions to

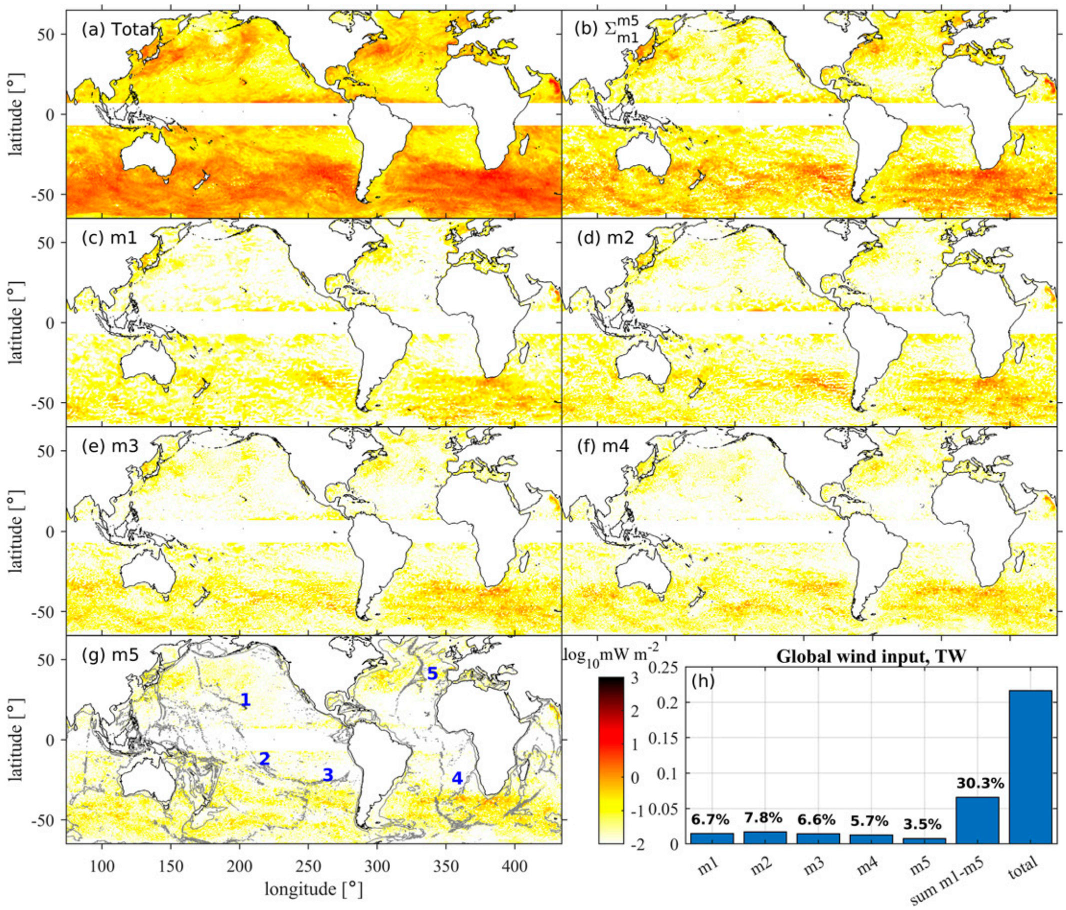

FIG. 1. Time-mean, near-inertial surface wind power input to (a) the undecomposed fields, (b) sum of modes 1–5, and (c)–(g) modes 1–5. (h) Global integral of wind power input (numbers above the bars indicate the fraction of the undecomposed near-inertial wind input). The 2500-m seafloor depth is plotted as a gray contour in (g), to illustrate major oceanic ridges such as the 1: Hawaiian–Emperor seamount chain, 2: French Polynesian islands, 3: Salas y Gómez and Nazca Ridges, 4: Walvis Ridge, and 5: Azores Plateau.

the first five modes accounts for only 30.3% (0.064 TW/0.210 TW) of the undecomposed near-inertial wind power input. The remaining 69.7% (0.146 TW/0.210 TW) of near-inertial wind power input goes to motions not resolved by modes 1–5, surface near-inertial oscillations, and/or mixed layer turbulence.

b. *NIW energy*

To better understand patterns of NIW energy and NIW propagation pathways, we present the depth-integrated, time-mean NIW energy E for the undecomposed fields, modes 1–5, and their sum in Fig. 3. The zonally averaged NIW energy in the modal and the undecomposed fields are shown in Fig. 2b. The global distribution of NIW energy and its zonal mean shows similar patterns as the wind input in Figs. 1 and 2a. Most of the undecomposed and modal NIW energy resides in the Southern Ocean with higher values in regions south of Africa and west of South America, corresponding to a higher wind input. There is enhanced NIW energy in the western boundary current regions (~40°N) where high mesoscale activity contributes to more wind power input. The global depth and area integrated NIW energy for the undecomposed fields is 224 PJ, of which the kinetic energy makes up 85.6% and the available potential energy make up 14.4%.

The higher NIW energy in the North Pacific Ocean region that appears in the undecomposed fields and the higher modes is most likely due to thermobaric instability (TBI; Buijsman et al. 2020). TBI is a numerical instability that can occur in ocean models with isopycnal coordinates due to imperfect compensation for compressibility in the pressure gradient term. The pressure gradient errors can cause the coordinate interfaces in weakly stratified regions to migrate in a way that amplifies the pressure gradient errors, leading to an exponentially growing instability (Hallberg 2005). The disturbances due to TBI have a broadband nature and they do not correlate well with the surface wind stress. Hence, they have a minimal impact on the wind power input fields in Fig. 1. However, TBI generates near-inertial band motions that mostly project on modes 3 and higher. The regions with TBI identified by the blue polygons in Fig. 3 are excluded for

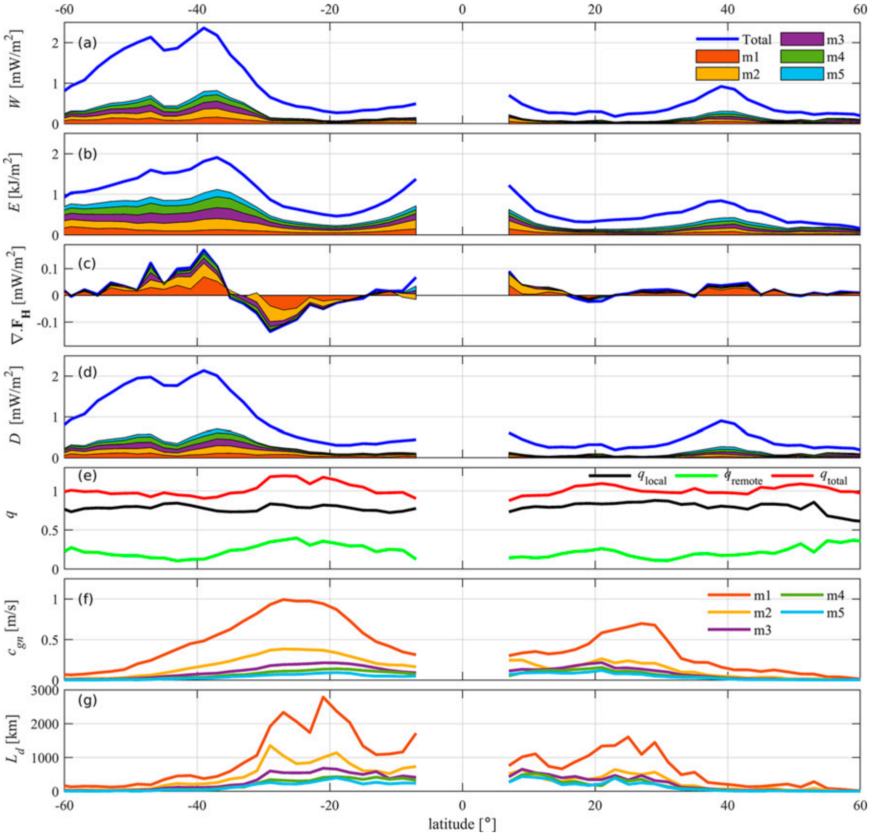

FIG. 2. Zonal averages of near-inertial (a) wind input; (b) energy density; (c) divergence of horizontal energy flux; (d) dissipation; (e) locally dissipated fraction q_{local}, remotely dissipated fraction q_{remote}, and total (local + remote) dissipated fraction q_{total}; (f) modal group velocities; and (g) modal decay length scales. In (a)–(d), the thickness of each colored layer corresponds to the energy/power of each mode and the blue line reflects the energy/power of the undecomposed fields.

the undecomposed fields and modes ≥3 in the calculation of global energy integrals and other diagnostics. The correction of TBI in the model is beyond the scope of this paper. Hallberg (2005) discusses various methods by which TBI can be avoided in ocean models.

The modal partitioning of the global depth and area integrated NIW energy is shown in Fig. 3h. Similar to the wind input, mode 1 is not the most energetic near-inertial mode in the global ocean. It makes up only 10.1% of the undecomposed energy. The NIW energy in each resolved mode is about equal (modes 2–4 have higher energies than mode 1), reflecting the nearly equal wind power input to these modes (Fig. 1h). The sum of NIW energy in the first five modes amounts to 58% (130 PJ/224 PJ) of the undecomposed NIW energy. The remaining 42% of the undecomposed NIW energy goes to unresolved high wavenumber motions and surface near-inertial oscillations. The fraction of undecomposed energy going to the first five modes is higher than the fraction of the total near-inertial wind power input to the first five modes (58% and 30.3%, respectively; cf. Figs. 3h and 1h). This suggests that a significant portion of surface near-inertial wind power input goes to mixed layer deepening and dissipation, instead of NIW energy (Alford 2020b).

c. Horizontal propagation of NIWs

In this section, we evaluate the horizontal energy flux patterns for the undecomposed and modal fields. The depth-integrated, time-mean NIW horizontal energy fluxes $\mathbf{F}_H$ for the undecomposed fields are presented in Fig. 4a (vectors) along with the time-mean near-inertial wind power input (in color). The mode 1 fluxes are shown in Fig. 4b. Strong near-inertial fluxes are directed toward the equator from regions of high wind input in both the hemispheres. In the Northern Hemisphere, both the Kuroshio and Gulf Stream have strong wind input that cause large fluxes of about 100 W m^{-1}. The NIW energy fluxes are the strongest in southeast Pacific (~500 W m^{-1}) and the Southern Ocean (~300 W m^{-1}) where the wind input is large.

Although most of the mode-1 fluxes are directed toward the equator in Fig. 4b, not all low-mode fluxes reach the equator, but rather get reflected, scattered, and/or dissipated at the east–west-oriented midocean ridges such as the Hawaiian–Emperor seamount chain in the North Pacific, Azores Plateau in the North Atlantic Ocean, the French

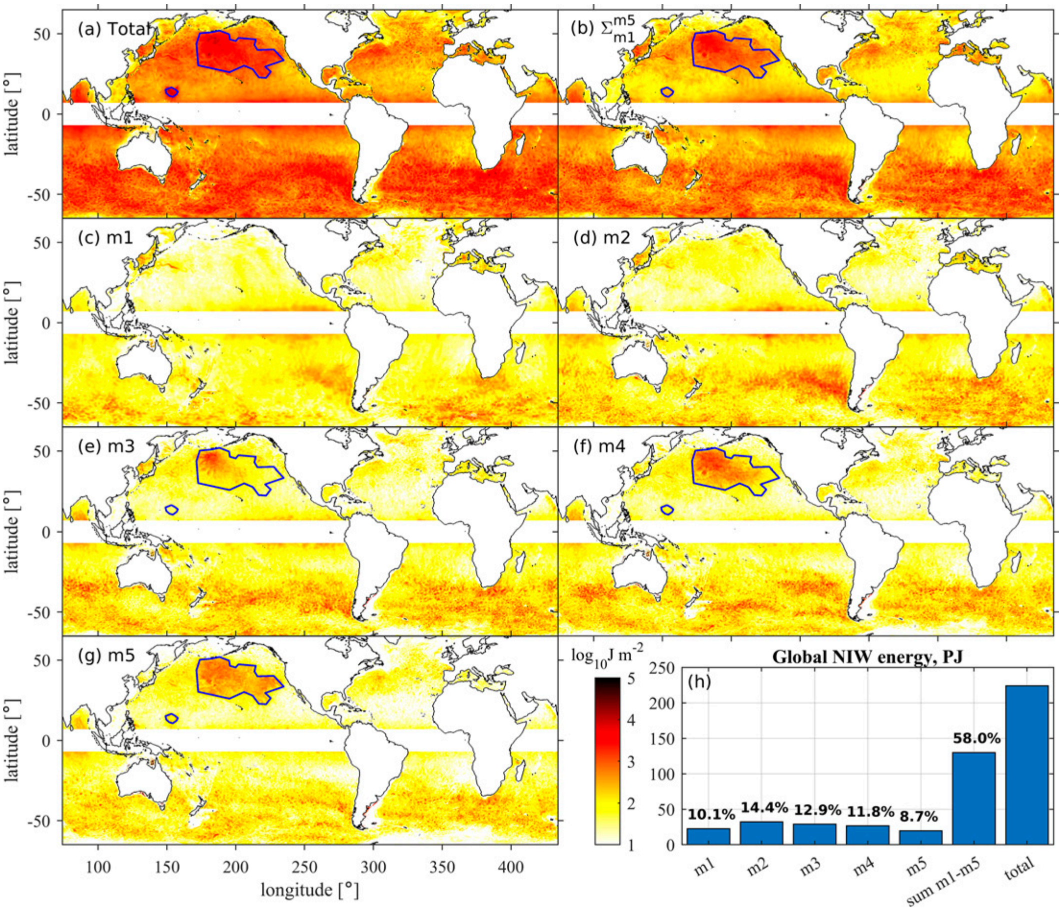

FIG. 3. As in Fig. 1, but for the depth-integrated, time-mean NIW energy *E*. The areas enclosed by the blue polygons are regions with TBI and are excluded from calculating global integrals.

Polynesian islands, the Salas y Gómez and Nazca Ridges in the South Pacific, and the Walvis Ridge off the coast of Namibia in the southeast Atlantic (Fig. 4b; the ridges are labeled in Fig. 1g). Notably, the ~2900-km-long Salas y Gómez and Nazca Ridges that extend westward from the west coast of South America (~25°S) block an average equatorward energy flux of 495 W m^{-1}. Together with the French Polynesian islands, the Salas y Gómez and Nazca Ridges form a barrier for the equatorward propagation of NIW fluxes in the South Pacific Ocean between 180° and 290°W, blocking about 75% of the equatorward mode-1 fluxes.

Strong northward and diverging fluxes occur in the northern Pacific south of the Aleutian islands in Fig. 4a without any corresponding wind power input (Fig. 1a). These fluxes are due to TBI and mostly project on higher modes and not on mode 1 (Fig. 4b). The broadband disturbances associated with the TBI have superinertial frequencies that allow for poleward propagation.

We compare the undecomposed and modal flux patterns in Fig. 5 for the Gulf Stream region. The sum of the fluxes in the first five modes is about 98.7% of the undecomposed flux in the global ocean (see Table 1 for the ratio for each mode). This means that we capture most of the horizontally propagating NIWs with the first five modes. Thus, the NIW energy that is not projected on the first five modes (42% of the total NIW energy) is associated with nonpropagating surface near-inertial motions and higher wavenumber waves that also propagate vertically. The mode-1 flux clearly dominates among the first five modes, in contrast to the modal distributions of *E* and *W*. While the mode-1 fluxes are directed equatorward and have coherent patterns, fluxes in modes 2 and higher have more chaotic flux patterns. A possible explanation for these chaotic patterns is that higher modes are more strongly refracted by the background flow than lower modes (Rainville and Pinkel 2006; Zaron and Egbert 2014).

We compute depth-integrated horizontal flux divergences to show sources and sinks of NIW energy. Instead of showing noisy global maps, we discuss the zonal means of the total and modal flux divergence shown in Fig. 2c. The zonally averaged flux divergence of modes 1–5 nearly sums up to the undecomposed flux divergence for all latitudes. The flux divergences of modes 1 and 2 are much higher than that for modes 3–5. Low-mode NIWs propagate away from higher latitudes (e.g., >|40°|) where flux divergence is positive and converge in lower latitudes (e.g., <|30°|) where the divergence is negative. In the Southern Hemisphere, modes 1 and 2 have high negative divergence at around 30°S owing to their reflection and eventual dissipation at midocean ridges such

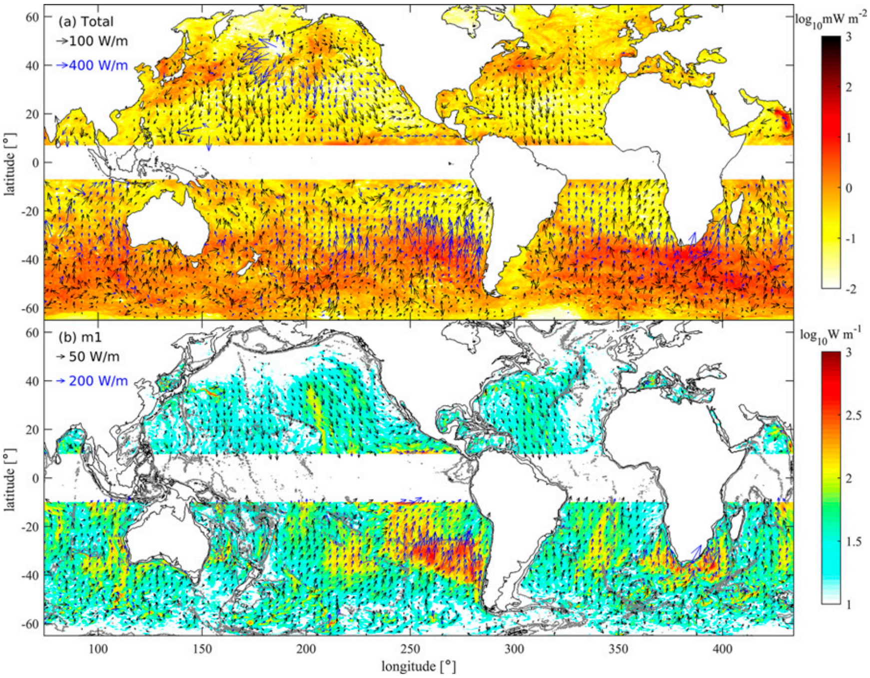

FIG. 4. Depth-integrated, time-mean NIW horizontal energy flux (vectors) for the (a) undecomposed (total) and (b) mode-1 fields. The color shadings represent the time-mean near-inertial surface wind power input in (a) and the magnitude of mode-1 flux in (b). The black and blue vectors respectively represent fluxes with a magnitude less than and greater than 100 W m^{-1} in (a) and 50 W m^{-1} in (b). The fluxes with magnitudes less than 10 W m^{-1} are not shown.

as the Salas y Gómez, Nazca, and Walvis Ridges. At the onset of the northern summer, the zonal-mean flux divergence in the Northern Hemisphere is smaller than in the Southern Hemisphere, with a minor peak close to 40°N where the wind input has a maximum in the western boundary currents.

d. Dissipation of NIWs

The time-mean and zonally averaged NIW dissipation, that is, the residual calculated from the energy balance Eqs. (1) and (9), is presented in Fig. 2d. Peaks in the dissipation agree well with the peaks in energy and wind input in Figs. 2a and b. Indeed, most of the wind power input is dissipated at the same latitude. The remainder propagates away as low-mode waves that dissipate at lower latitudes. Since the zonally averaged horizontal flux divergence is only around 5% of the wind input in most latitudes, we may say that zonally averaged D is almost equal to zonally averaged W.

The locally dissipated fraction of internal wave power input, $q_{\mathrm{local}} = D_{\mathrm{local}}/I$ (where D_{local} is the local dissipation rate and I is the internal wave power input associated with barotropic to baroclinic tide conversion or wind power input) is used to parameterize the internal wave driven mixing in the ocean (MacKinnon et al. 2017). Although q_{local} is generally evaluated for internal tides, Alford (2020a) recently discussed the calculation of q_{local} for NIWs in the global ocean. Following Vic et al. (2019), Alford (2020a) assumes that NIW modes 1–3 propagate away and modes 4–20 contribute to local dissipation. Using this assumption, Alford (2020a) computes global-mean q_{local} values of 0.63 and 0.75 for winter and summer, respectively. We compute the locally dissipated fraction in our model for the duration of 30 days and compare with the seasonal-mean values of Alford (2020a).

The choice of the cutoff mode number to define the propagating component of the wind input depends on the definition of "local." With the horizontal resolution of ~4 km in our simulation, all the resolved modes propagate out of the grid cell where they are generated. However, maps of q_{local} at 4-km resolution are noisy. To reduce the grid-scale noise and to better visualize the spatial trends, we compute q_{local} in 2° × 2° bins. We can estimate the distance traveled by the modes before they are dissipated by the average decay length scales L_d for modes given by Eq. (12). The L_d for modes 4 and 5 are $O(100\ \mathrm{km})$ or <2°, whereas the L_d for modes 1–3 are $O(1000\ \mathrm{km})$, as shown in Fig. 2g. Hence, we choose mode 3 as the cutoff to define the propagating component of the wind input. However, in contrast to the computation of Alford (2020a), we assume that all the wind input that does not project on modes 1–3 contributes to local dissipation, since it is not available for propagating NIWs. Thus, we compute the locally dissipated fraction as

$$q_{\mathrm{local}} = \frac{W - \sum_{n=1}^{3} W_n}{W}. \tag{13}$$

The locally dissipated fraction q_{local} is presented in Fig. 6a, and its zonal average is presented in Fig. 2e (black curve).

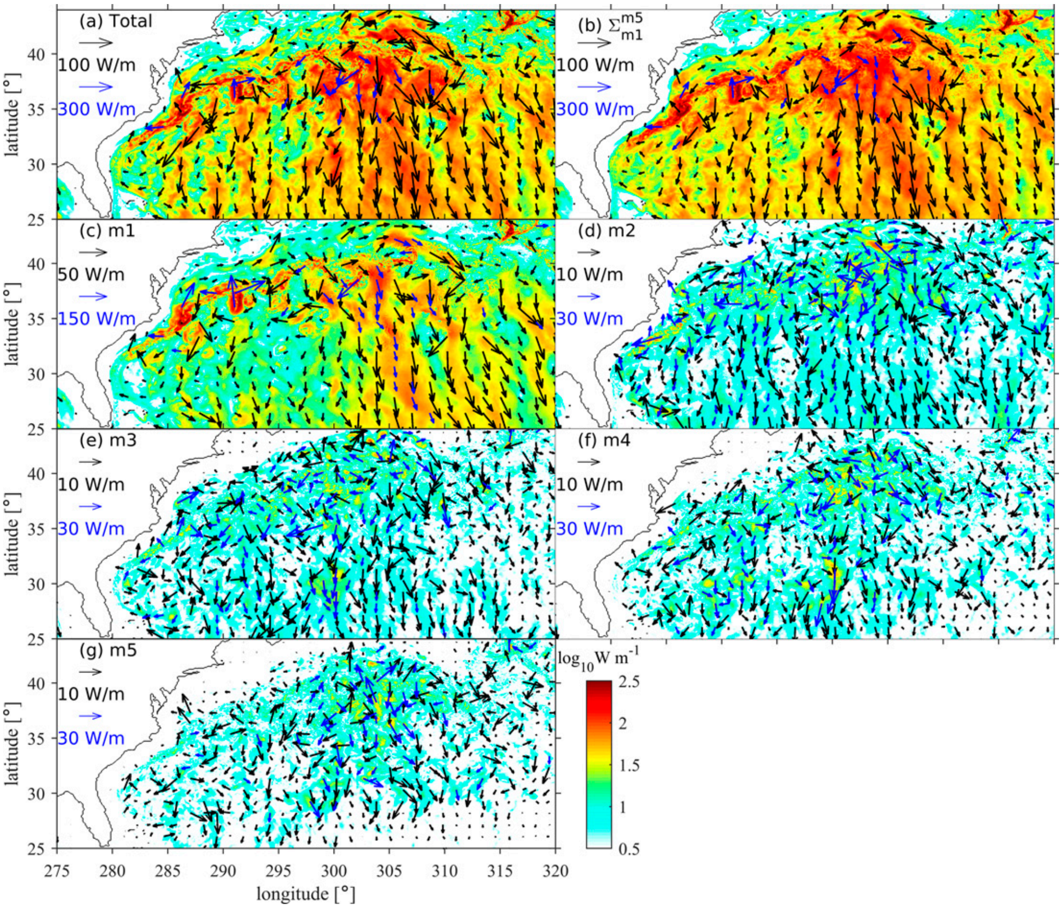

FIG. 5. Depth-integrated near-inertial horizontal energy fluxes $\mathbf{F}_H$ for (a) the undecomposed fields, (b) sum of the first five modes, and (c)–(g) modes 1–5. The magnitude of the flux is shown in color shades. Blue vectors show fluxes with a magnitude larger than 100 W m^{-1} in (a) and (b), 50 W m^{-1} in (c), and 10 W m^{-1} in (d)–(g).

The distribution of q_{local} is largely uniform throughout the ocean. We obtain a global mean value of $q_{\text{local}} = 0.79$ for the period of May–June, which is comparable to the estimates of q_{local} for summer by Alford (2020a).

The dissipation of near-inertial energy at any location in the ocean not only includes the dissipation of locally generated NIWs but also the dissipation of remotely generated NIWs that have propagated there. We can calculate a remotely dissipated fraction as

$$q_{\text{remote}} = \frac{D - \left(W - \sum_{n=1}^{3} W_n\right)}{W}. \tag{14}$$

TABLE 1. The ratio of the area-averaged flux magnitudes of the near-inertial modes to the area-averaged flux magnitudes of the undecomposed fields in the global ocean.

n	1	2	3	4	5	$\sum_{n=1}^{5}$
$\lvert\mathbf{F}_n\rvert/\lvert\mathbf{F}_H\rvert$	50.5%	28.9%	11.6%	5.7%	2.0%	98.7%

The global distribution of q_{remote} is shown in Fig. 6b. The value of q_{remote} is higher at the lower latitudes ($<|30°|$) particularly near many oceanic ridges. The strong NIW fluxes generated at the higher latitudes of the Southern Hemisphere propagate equatorward and dissipate at the lower latitudes. The region west of South America has very high q_{remote} at around 30°S, owing to the reflection and dissipation of low-mode NIWs at the Salas y Gómez and Nazca Ridges; q_{remote} is also higher at the French Polynesian islands in the South Pacific and the Walvis Ridge in the South Atlantic. The zonally averaged q_{remote} in Fig. 2e (green curve) reflects the map in Fig. 6b. The latitudes where the zonally averaged q_{remote} is high corresponds with the latitudes where the flux divergence is negative (see Fig. 2c).

We also show the zonal average of $q_{\text{total}} = q_{\text{remote}} + q_{\text{local}} = D/W$ in Fig. 2e (red curve). The zonally averaged q_{total} has values less than 1 at higher latitudes and increases to above 1 at low latitudes. In the regions where $q_{\text{total}} > 1$, the near-inertial dissipation exceeds the local wind input due to the dissipation of remotely generated NIWs. This analysis shows that the contribution of remote waves should not be ignored when developing parameterizations for internal wave driven mixing in the ocean.

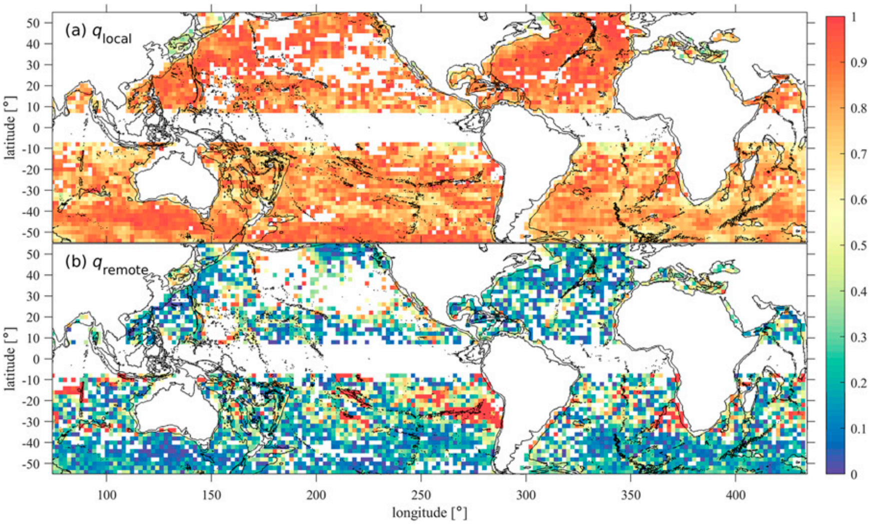

FIG. 6. (a) The locally dissipated fraction q_{local} (global mean = 0.79) and (b) the remotely dissipated fraction q_{remote}. The 0- and 2500-m seafloor depths are plotted as black contours.

Low-mode NIWs transport near-inertial energy from higher to lower latitudes. The speed of energy propagation is determined by the group speed. We compute the group speed $c_{g,n}$ for modes 1–5 using Eq. (11) and present the zonally averaged group velocity in Fig. 2f. Mode 1 has the highest $c_{g,n}$, almost 2 times the mode-2 speed. In both hemispheres, the values of $c_{g,n}$ for modes 1 and 2 increase toward the lower latitudes with a peak at about |25°| before decreasing toward the equator. The decrease toward the equator may be attributed to increased dissipation at midocean ridges and/or the way the group speed is calculated, that is, it depends on waves that are generated at different latitudes with different theoretical group speeds. In Fig. 2g, L_d is largest for mode 1, with higher modes having gradually smaller values. The peaks of L_d correspond to the zonally averaged flux divergence in Fig. 2c, with regions of negative flux divergence having high L_d. Thus, low-mode NIWs with larger $c_{g,n}$ and L_d travel from higher latitudes to lower latitudes, where they dissipate.

e. *Influence of background vorticity*

The horizontal propagation of NIWs is not only affected by the gradients in planetary vorticity but also by the gradients in relative vorticity of the background flow, which shifts the local inertial frequency as $f_{\text{eff}} = f(1 + 0.5\zeta/f)$ (Mooers 1975; Kunze 1985). In this section, we examine the influence of background relative vorticity on the undecomposed and modal NIW energy propagation and dissipation in the global ocean.

The 30-day mean surface vorticity normalized by local f is shown in Fig. 7a. The positive values correspond to cyclonic and negative values correspond to anticyclonic vorticities. Large mesoscale eddies occur throughout the ocean with stronger vorticities associated with major ocean currents such as the western boundary and Agulhas Currents. The regions with strong mesoscale eddies coincide with areas of enhanced near-inertial wind power input (cf. with Fig. 4). A notable exception is the region west of South America, where a weaker vorticity field coincides with strong wind input due to local storms.

We examine the distribution of the undecomposed and modal near-inertial wind input, NIW kinetic energy, horizontal flux divergence and dissipation as a function of binned vorticity (Fig. 8). We discuss the distribution of KE (instead of E) with respect to vorticity because the distribution of APE is noisy. The energy terms are area averaged in normalized vorticity bins with a size of $\Delta\zeta/f = 0.05$ for the global ocean poleward of |7°| and excluding the regions with TBI. To better isolate the vorticity effect on each mode, we also present the normalized energetics in the right column of Fig. 8. The wind input, kinetic energy, and dissipation (Figs. 8b,d,h) are normalized by the total area-averaged wind input, kinetic energy and dissipation in each mode or the undecomposed fields, respectively. The flux divergence (Fig. 8f) is normalized by the root-mean-square flux divergence in each mode or the undecomposed fields.

The modal wind input in Figs. 8a and 8b does not show any correlation with the sign of background vorticity. The distribution of wind power input as a function of normalized vorticity is similar for all modes. The wind input in modes is higher in areas with higher vorticity (positive or negative). The wind input to the undecomposed fields (black curves in Figs. 8a,b) is slightly higher in cyclonic eddies than in anticyclonic eddies.

The depth-integrated modal NIW KE as a function of background vorticity is shown in Fig. 8c and 8d. The KE of the undecomposed fields (black curves in Figs. 8c,d) clearly shows preference to anticyclonic eddies. We see in Fig. 8d that for KE, higher modes correlate more strongly with the normalized vorticity than lower modes, although all modes tend to be trapped in regions of anticyclonic vorticity.

Figures 8e and 8f show the divergence of NIW horizontal energy flux as a function of normalized background vorticity. The normalized flux divergence for all modes and for the

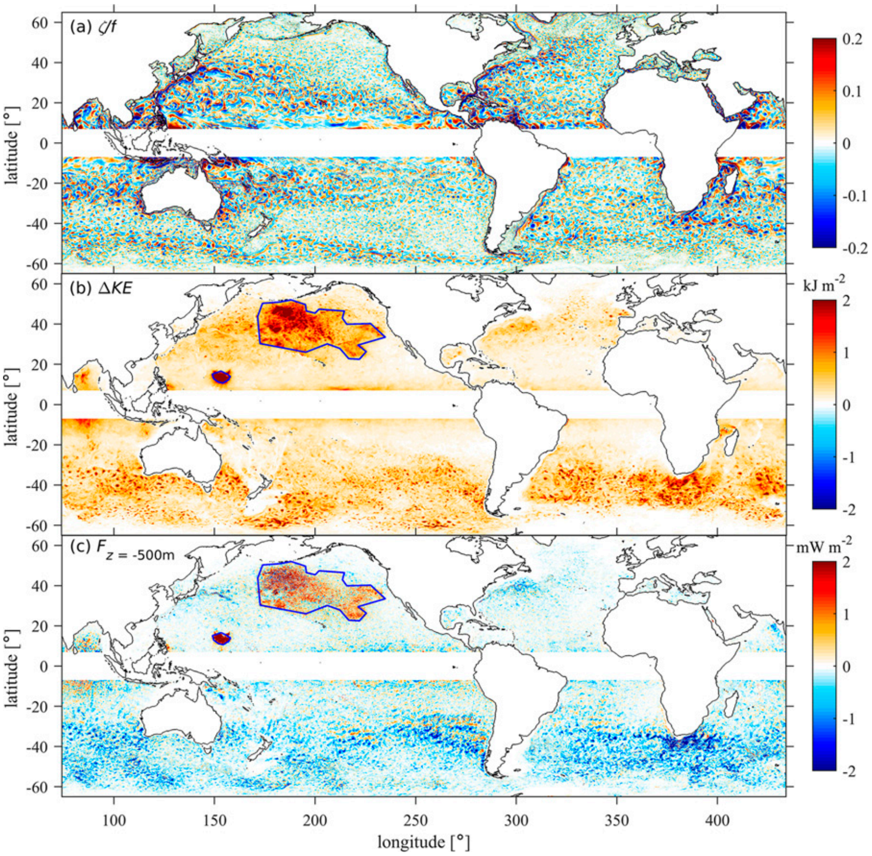

FIG. 7. Time-mean (a) surface vorticity ζ normalized by local f, (b) residual NIW kinetic energy ΔKE, and (c) NIW vertical energy flux F_z at $z = -500$ m. The areas enclosed by the blue polygons are regions with TBI and are excluded from the analyses.

undecomposed fields in Fig. 8f is positive for cyclonic vorticities and negative for anticyclonic vorticities. Similar to KE (Fig. 8d), negative normalized flux divergence of the high modes correlates more strongly with anticyclonic vorticity than the flux divergence of the lower modes. This clearly shows that globally, all resolved NIW modes propagate away from cyclonic eddies and toward anticyclonic eddies. In accordance with the fluxes in Fig. 5, the sum of the flux divergence of modes 1–5 agrees well with the undecomposed flux divergence for all vorticity values, further confirming that the first five modes include most of the horizontally propagating NIWs. Last, the dissipation of the undecomposed fields and the modes in Figs. 8g and 8h reflect the same trends as for W, KE, and $\nabla \cdot \mathbf{F}_H$; that is, NIW dissipation is biased toward the anticyclones. Our results from a global ocean simulation are in agreement with the observations of Whalen et al. (2018) and Sanford et al. (2021), who also found that near-inertial energy is concentrated in anticyclones.

The bin area as a fraction of the total surface area of the ocean is shown in Fig. 8b. We calculate that almost 66% of ocean surface area has $|\zeta/f| < 0.025$ and almost 90% of the ocean surface area has $|\zeta/f| < 0.01$. We see the strongest response of the NIW energy terms for the largest vorticity values, which occur for less than 10% of the ocean surface area. Nevertheless, the trends are clearly present for $|\zeta/f| < 0.1$.

f. Vertical energy flux

The difference between the undecomposed and modal kinetic energy, that is, the residual kinetic energy ΔKE, is 42% of the undecomposed kinetic energy. What is the fate of this energy? A global map of the ΔKE is shown in Fig. 7b. We see that ΔKE is mostly confined to anticyclonic eddy features, but the largest eddies do not necessarily have the highest ΔKE. The Southern Ocean has a high concentration of ΔKE, particularly to the south of Africa.

Since almost all of the horizontal fluxes are represented by the first five modes, the residual KE most likely reflects energy of high wavenumber waves that propagate vertically downward. Hence, we calculate the vertical flux of near-inertial energy. The vertical energy flux is given by $F_z = p'w$, where w is the near-inertial vertical velocity calculated offline using the continuity equation. The maximum mixed layer depths are shallower than 500 m in the global ocean during May–June 2019. Therefore, we calculate the vertical energy flux at $z = -500$ m to estimate NIW energy transmission to the deep ocean. We show the time-mean vertical flux of NIW energy at a depth of 500 m in Fig. 7c. Negative

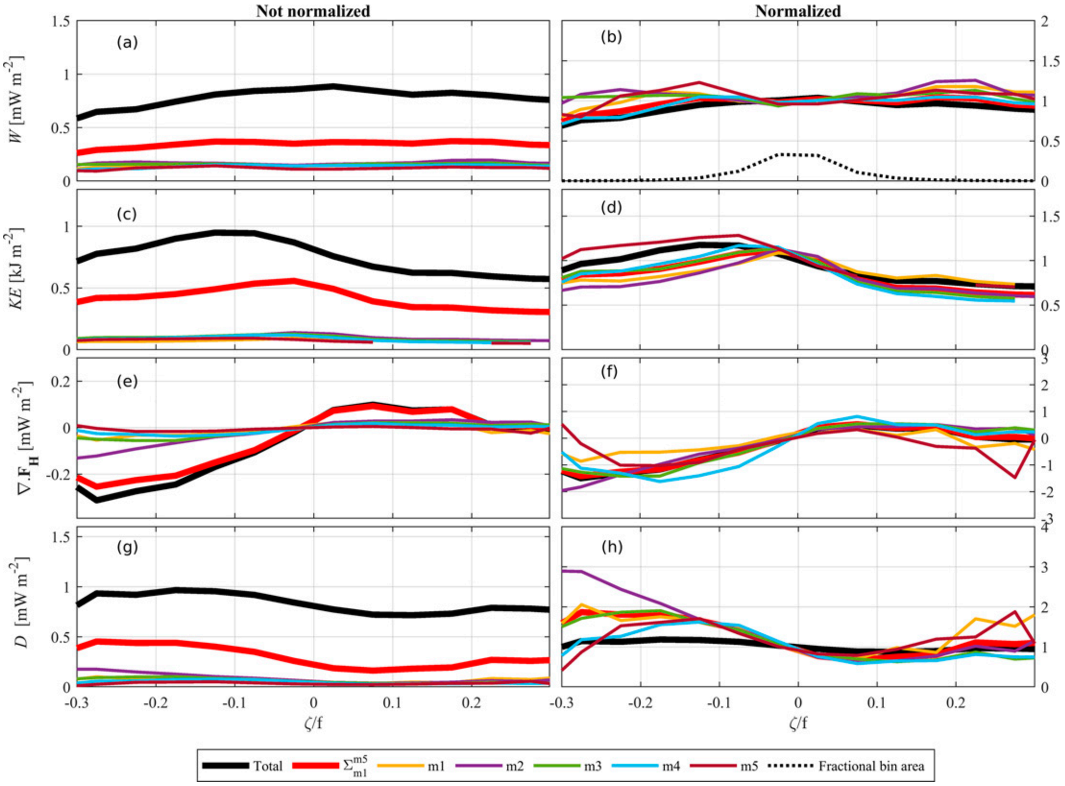

FIG. 8. The distribution of time-mean, area-averaged near-inertial (a),(b) surface wind power input; (c),(d) kinetic energy; (e),(f) divergence of horizontal energy flux; and (g),(h) dissipation as function of time-mean surface relative vorticity. The variables for the undecomposed fields are shown as thick black curves, and those for the sum of modes 1–5 are shown as thick red curves. The fractional bin area of the total ocean surface area of 2.3×10^8 km^2 is shown as a black dotted curve in (b). All values are area averaged for vorticity bins of $\Delta\zeta/f = 0.05$. In (b), (d), (f), and (h) the y axis variables are normalized as described in the text.

values indicate a downward energy flux. The NIW vertical flux is higher in regions with strong wind input (cf. with Fig. 4a), which are also regions of high mesoscale activity. We also find high NIW transmissions in the Southern Ocean that are mostly confined to anticyclonic eddies. The regions outlined by the blue polygons are regions with TBI, where the vertical energy fluxes are also positive, that is, TBI generates NIWs in the interior of the ocean that propagate toward the surface. We neglect the TBI regions in our calculations. In our simulation, the area-integrated near-inertial power that is transmitted below $z = -500$ m is 0.04 TW (19% of the surface wind power input). Thus, most of the wind power (81%) is dissipated in the top 500 m of the ocean.

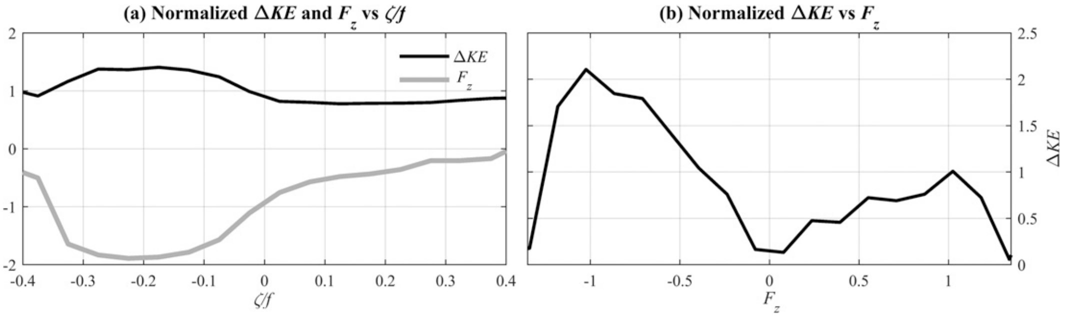

FIG. 9. (a) The distribution of the time-mean depth-integrated, normalized residual kinetic energy ΔKE and vertical energy flux F_z at $z = -500$ m as a function of the time-mean surface relative vorticity ζ/f. Values are area-averaged for vorticity bins of $\Delta\zeta/f = 0.05$. (b) The distribution of the time-mean normalized ΔKE as a function of normalized F_z. The ΔKE and F_z are normalized by their root-mean-square values.

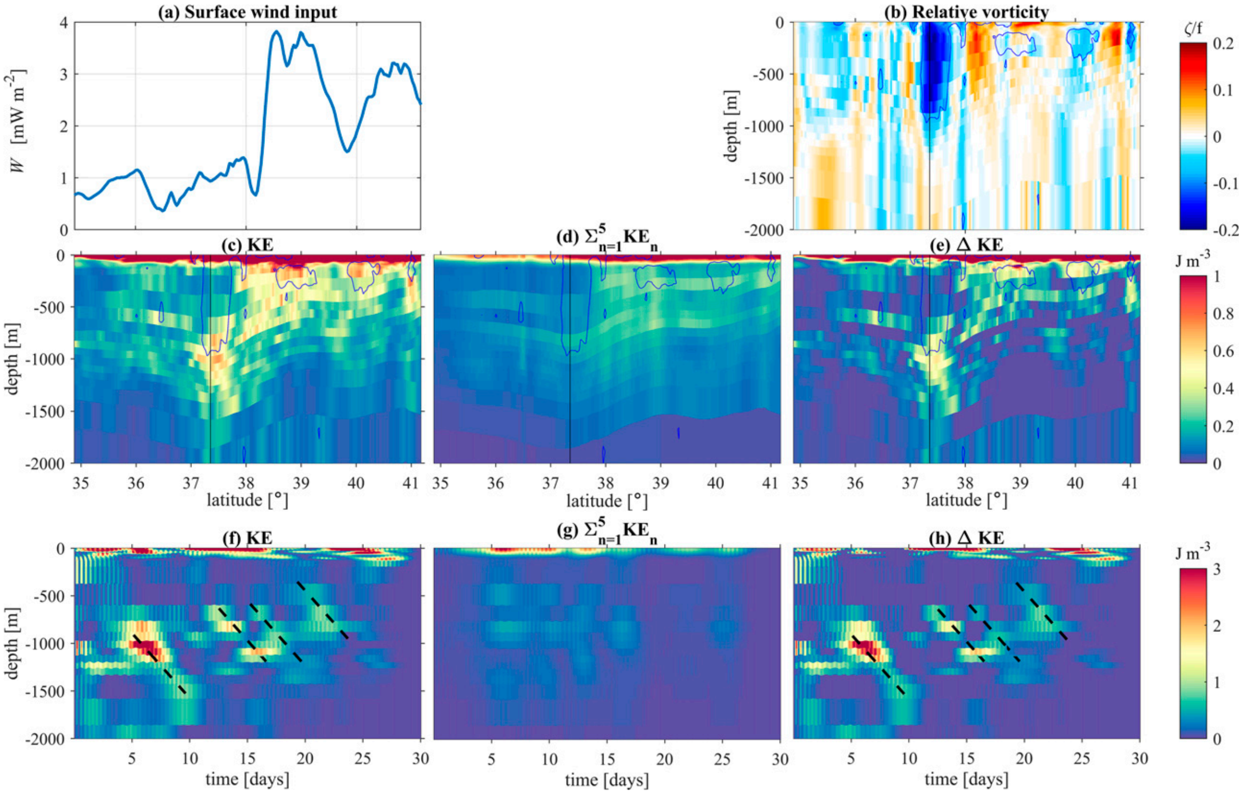

FIG. 10. Time-mean (a) surface wind input, (b) relative vorticity, (c) KE, (d) sum of KE in first five modes, and (e) ΔKE along a vertical transect at 300.5°W longitude. The blue contours enclose $\zeta/f < -0.1$, representing anticyclonic motions. Also shown are time series of (f) KE, (g) sum of KE in the first five modes, and (h) ΔKE near an anticyclone at 37.3°N, 300.5°W. The vertical profile for which the time series are extracted is shown with a thin vertical black line in (b)–(e).

Both normalized ΔKE and F_z correlate strongly with negative relative vorticity (Fig. 9a). The area-averaged ΔKE and F_z are normalized by their respective root-mean-square values. The residual KE that is not associated with horizontally propagating modes is trapped in anticyclonic eddies. The downward transmission is also strongest in anticyclonic eddies. Furthermore, in Fig. 9b, we find that the normalized ΔKE is higher when the vertical flux of NIW energy is negative (downward vertical flux). This clearly establishes that the vertical flux of NIW energy is associated with ΔKE.

VERTICALLY PROPAGATING NIWS: A CASE STUDY

The vertical propagation of NIW kinetic energy is further examined in an anticyclonic eddy. We take a vertical transect through an anticyclonic eddy at 37.3°N, 300.5°W in the Gulf Stream region. The transect runs from 35° to 41°N and includes a nearby region of strong wind input. Figure 10a shows the time-mean wind input along the vertical transect. The wind input has a peak at latitudes 38.5°–39.5°N. The relative vorticity in Fig. 10b shows the anticyclone near 37.3°N. The time-mean near-inertial KE in Fig. 10c is enhanced in the upper layers of the ocean in regions where the wind input is high, but is trapped at the base of the anticyclonic core near $z = -1000$ m. In contrast to the modal KE in Fig. 10d the residual KE in Fig. 10e shows a large variability at small horizontal and vertical scales. We compute a time-mean downward near-inertial flux of 0.068 W m^{-2} at $z = -500$ m at 38.5°N.

Figures 10f–h show the time series of the undecomposed KE, KE in modes 1–5 and residual KE at the location of the anticylonic eddy (37.3°N, 300.5°). The undecomposed KE has a maximum at $z = -1000$ m on day 5 and progresses downward as days pass. The downward propagation of KE is marked by dashed lines in Fig. 10f. The residual KE in Fig. 10h has a vertical structure associated with large vertical and horizontal wavenumber waves not captured by our modal analysis. From the downward propagation of KE, we compute a vertical group speed of −1.4 mm s^{-1} (−120 m day^{-1}).

The downward propagation of NIW KE is associated with short wavelength (large wavenumber) waves, as shown in Fig. 10. High wavenumber NIWs that do not project on vertical modes 1–5 are modulated more by the background eddies and are most likely to propagate downward as beamlike features in anticyclonic eddies. Numerous process modeling studies (Lee and Niiler 1998; Danioux et al. 2015; Asselin and Young 2020) and observations (Whalen et al. 2018; Thomas et al. 2020; Sanford et al. 2021) have established that background anticyclonic relative vorticity (negative ζ/f) enhance the vertical transmission of NIW energy, and that NIWs get trapped in anticyclonic eddies, where they ultimately dissipate.

4. Discussion

The primary purpose of this paper is to study the modulation of NIW energetics by the background flows in a global HYCOM simulation. For the first time in a global ocean simulation, we have examined the global spatial patterns of the time-mean and depth-integrated total, modal and residual NIW energy terms and studied how these energy terms are modulated by the background vorticity. We will now discuss our results in the context of previous model studies and discuss the merits and limitations of our simulation.

The analyses presented in this paper are for 30 days in May–June 2019. This period coincides with the cruises in the North Atlantic Ocean as part of Near Inertial Shear and Kinetic Energy in the North Atlantic experiment (NISKINe). Although 30 days of 3D data permits us to study the energetics of NIWs and their modulation by the background mesoscale vorticity, we do not capture much of the seasonality in the NIW dynamics. May–June, at the onset of boreal summer, has the lowest near-inertial wind power input in the global ocean, particularly in the Northern Hemisphere. In the Southern Hemisphere, May–June has a wind power input that is about 83% of the peak power input (Simmons and Alford 2012). Consequently, most of the NIW energy in our simulation is in the Southern Hemisphere. The low and high wind speed conditions in the Northern and Southern Hemispheres coincide with a significant range of stratification, mesoscale variability, and wind speeds in our simulation. Hence, we argue that our findings with respect to the vorticity modulation of NIW energy terms are representative and not unique to our simulation period.

Even though the horizontal and vertical resolution of our simulations is an improvement over past studies on global NIW energetics, our simulations fall short in fully resolving all the nonlinear interactions among waves themselves and between waves and (sub)-mesoscale flows. The resolution of our simulation (4 km in the tropics) is sufficient to resolve most of the mesoscale motions, but the submesoscales (~1.5 km; Morvan et al. 2020), where most of the nonlinear interactions take place, are not resolved in our simulations. Hence, we include all the energy transfers through nonlinear interactions in the dissipation term [D in Eq. (1)], assuming that all such interactions lead to motions that dissipate locally. Nevertheless, Müller et al. (2015) studied spectral energy transfers in a HYCOM simulation with similar configuration as ours, and they have been able to reproduce low vertical-mode internal wave triad interactions. In a subsequent study, Ansong et al. (2018) analyzed the global distribution of PSI of internal tides in 4-km HYCOM simulations. We too find some evidence of nonlinear interactions in our simulation with tides, which is discussed in the appendix.

Our study shows that the modal partitioning of the depth-integrated energy for NIWs is in stark contrast to the modal partitioning for M_2 internal tides. For M_2 internal tides (see Fig. 9c in Buijsman et al. 2020), the depth-integrated energy in mode 1 is 56.2% (86 PJ/153 PJ) of the sum of energy in modes 1–5, whereas for NIWs the energy in mode 1 makes up only 17.7% (23 PJ/130 PJ) of the sum of energy in modes 1–5. Consequently, the energy in modes 2–5 for NIWs (107 PJ) is about 1.6 times as high as for M_2 internal tides (67 PJ). From these results, we can conclude that while the long propagating low-mode internal wave energy is dominated by internal tides, the high-mode internal wave energy that is relevant for mixing is dominated by NIWs. This difference in modal partitioning of energy between internal tides and NIWs has also been noted in observations by Alford (2010).

Although energetically weaker than internal tides, we do find NIWs that propagate equatorward over long distances (Fig. 4b) in our simulation. The ratio of the undecomposed fluxes that radiate equatorward of |30°| to the wind input for latitudes $>$ |30°| is 9.8% (1.4 GW/14.7 GW) in the Northern Hemisphere and 3.0% (4.6 GW/153.6 GW) in the Southern Hemisphere, resulting in a global value of 3.6%. The ratio we calculate for May–June is less than the annual mean ratio of 7% calculated by Furuichi et al. (2008) and falls in the lower end of the annual range of 2%–16% given by Simmons and Alford (2012). The lower ratio of equatorward radiation in our simulation may be due to a higher model resolution that facilitates more nonlinear interactions, the inclusion of wave drag in HYCOM, the presence of background flows, and a more realistic topography, which may block and reflect NIWs (e.g., at the Salas y Gómez and Nazca Ridges in the South Pacific Ocean).

The vertical transmission of NIW energy into the ocean interior in our simulation is in alignment with previous model studies. The area-integrated vertical flux of near-inertial energy at 500-m depth is 0.04 TW (19% of the surface wind power input). Hence, 81% of the wind power input is dissipated in the top 500 m of the ocean. Furuichi et al. (2008) found that about 75%–80% of surface near-inertial wind input is dissipated in the top 150 m using a model without eddies. Rimac et al. (2016) estimated that only 10% of wind power is transmitted below the surface mixed layer in a model simulation with mesoscale eddies. We find a greater proportion of NIW energy transmission to the ocean interior in HYCOM, possibly due to better horizontal resolution of 1/25°, better resolved mixed layer, and more frequent wind forcing (3 hourly) in our model. The higher percentage of downward flux in our study can also be due to the lower wind input in May–June. The observations by Alford et al. (2012) show that the downward flux of NIW energy at 800 m can vary between 12% and 33% depending on the seasonal variation of the wind input. In a future paper, we will study the vertical propagation and dissipation of NIW energy as a function of depth in more detail.

5. Conclusions

We have studied the depth-integrated energetics of NIWs in realistically forced eddying global HYCOM simulations during 30 days in May–June 2019. We have determined what fraction of total near-inertial wind input, energy, and dissipation can be attributed to the resolved vertical modes. We have examined the global spatial patterns of the total, modal, and residual NIW energy terms and studied how these energy terms are modulated by the background vorticity. We list the main findings from our analyses below:

- The wind input in the first five modes adds up to only 30.3% of the total near-inertial wind input. However, the NIW energy in the first five modes adds up to about 58% of the total NIW energy. This difference in modal projections may imply that a significant portion of surface wind input goes to the deepening of mixed layer and is not available for near-inertial motions as suggested by Alford (2020b).
- Almost all of the depth-integrated NIW horizontal energy flux projects on the first five modes. Hence, the residual energy that does not project on the first five modes is associated with near-inertial motions that do not propagate horizontally.
- The low-mode NIW fluxes diverge from higher latitudes (e.g., $>|40°|$) and converge in lower latitudes (e.g., $<|30°|$). The equatorward propagation of low-mode NIWs is impeded at many of the east–west-oriented midocean ridges, where these NIWs reflect, scatter, and/or dissipate.
- The locally dissipated fraction of NIW energy q_{local} is found to be uniform throughout the global ocean with a global mean value of $q_{\mathrm{local}} = 0.79$. Additionally, we compute a remotely dissipated fraction q_{remote}. The value of q_{remote} is higher at the lower latitudes ($<|30°|$) than at the higher latitudes, in particular near the east–west-oriented oceanic ridges.
- The energy and energy flux divergence are strongly modulated by background vorticity. Most of the horizontal energy flux converges in anticyclones. High modes are more affected by the background eddies than low modes. We observe these trends for low vorticity values ($|\zeta/f| < 0.1$), which coincide with 90% of the global ocean surface area. The residual kinetic energy, ΔKE, (42% of total) is mostly concentrated in anticyclonic eddies. Most of this energy propagates downward, likely as waves with high horizontal and vertical wavenumbers.
- The global near-inertial wind power input for a 30-day period in May–June 2019 is 0.21 TW. Of this, only 0.04 TW (19% of the surface wind power input) is transmitted below 500-m depth. Most of the wind power input (81%) is lost in the upper layer processes of the ocean and is not available for deep ocean mixing.

Acknowledgments. This work was supported by the Office of Naval Research through NISKINe project Grants N000141812801 (Buijsman and Raja), N0001420WX01883 (Shriver), and N000141812544 (Arbic). We thank the editor and three anonymous reviewers for helpful suggestions to improve the presentation and interpretation of our results.

Data availability statement. The global time-mean near-inertial fields of modal and undecomposed wind input, depth-integrated kinetic and available potential energies, and depth-integrated horizontal energy fluxes for EXPT 19.2 are published online (https://zenodo.org/record/5765439).

APPENDIX

HYCOM Simulation with Tidal Forcing

In this section, we examine the HYCOM simulation EXPT 19.0, which is similar to EXPT 19.2 except with the inclusion of tidal forcing, and we discuss the difference in the global distribution of NIW kinetic energy with the addition of tides. Both experiments have the same wind forcing. We extract near-inertial fields from the experiments after removing stationary tides with a harmonic analysis and by applying a bandpass filter as explained in section 2b. The difference between the depth-integrated, time-mean, near-inertial kinetic energies of EXPT 19.0 and EXPT 19.2 ($\mathrm{KE}_{19.0} - \mathrm{KE}_{19.2}$) is shown in Fig. A1a, and the zonally averaged difference of kinetic energies (excluding TBI regions) is presented in Fig. A1b. We identify several differences between the experiments. The diurnal (D_1) internal tides are not perfectly removed in EXPT 19.0 (with tides) in particular in the western Pacific where D_1 internal tides are the strongest. In EXPT 19.0, the M_2 internal tides and NIWs interact nonlinearly via PSI near the critical latitudes ($\sim|30°|$) where the near-inertial frequency coincides with the diurnal frequency, leading to enhanced NIW energy, mostly in the western Pacific. The TBI is slightly worse in EXPT 19.2 (without tides) than in EXPT 19.0. The difference map in Fig. A1a has a noisy appearance because eddies that trap NIW kinetic energy occur in slightly different locations in the two experiments, in particular in the Southern Ocean and the western boundary currents. Although EXPT 19.0 has enhanced NIW kinetic energy in the western Pacific and near the critical latitudes, globally, EXPT 19.0 has less NIW kinetic energy ($\mathrm{KE}_{19.0}$ = 177.5 PJ) than EXPT 19.2 ($\mathrm{KE}_{19.2}$ = 191.8 PJ), excluding TBI regions. The reason for this difference is not directly clear, but in the simulation with tides, internal tides, and NIWs can interact nonlinearly and scatter energy to higher harmonics.

Near the critical latitudes, the nonlinear interactions between semidiurnal internal tides and NIWs result in enhanced energy in the near-inertial frequency band in the western Pacific to the west of Hawaii near 30°N in EXPT 19.0 (Figs. A1a,b). To further highlight the difference between the no-tides and tides simulations, we show the difference in velocity rotary spectra ($S_{19.0} - S_{19.2}$) at 30°N, 152°E in the western Pacific, where we expect PSI, in Fig. A1c. EXPT 19.0 has higher energy at the near-inertial frequency (positive values in Fig. A1c indicate higher energy in EXPT 19.0). PSI of the semidiurnal internal tides can effectively transfer energy of low-mode semidiurnal internal tides to high-mode near-inertial waves, which has been observed in the ocean (Van Haren 2005; Xie et al. 2011). The nonlinear interaction of M_2 internal tides and NIWs near critical latitudes can also excite waves at sum and difference frequencies of f and M_2 (Liang et al. 2019). In Fig. A1c, EXPT 19.0 has higher energy at the f, M_2, and $f + \mathrm{M}_2$ frequencies. This suggests the occurrence of nonlinear resonant interactions between NIWs, M_2 internal tides, and the $f + \mathrm{M}_2$ harmonic.

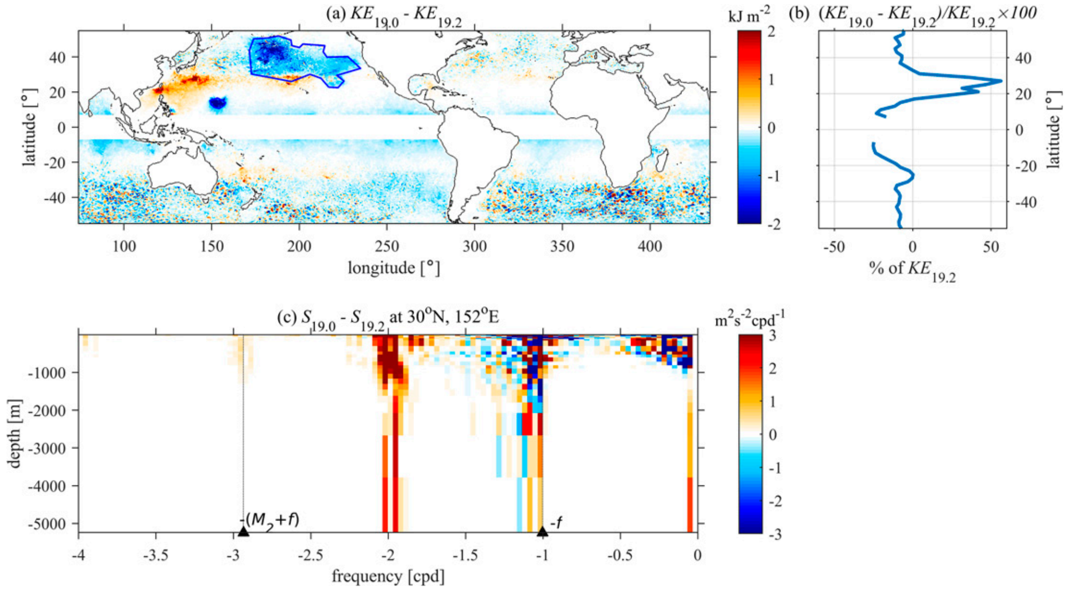

FIG. A1. (a) The difference of near-inertial kinetic energy between EXPT 19.0 (with tides) and EXPT 19.2 (without tides). (b) The zonally averaged difference of energy between EXPT 19.0 and EXPT 19.2. (c) The difference in velocity rotary spectra for EXPT 19.0 (with tides) and EXPT 19.2 (without tides) at 30°N, 150°E (PSI and $M_2 + f$ interaction region). The local f and $M_2 + f$ frequencies are shown by dashed lines.

REFERENCES

Alford, M. H., 2001: Internal swell generation: The spatial distribution of energy flux from the wind to mixed layer near-inertial motions. *J. Phys. Oceanogr.*, **31**, 2359–2368, https://doi.org/10.1175/1520-0485(2001)031<2359:ISGTSD>2.0.CO;2.

——, 2003: Improved global maps and 54-year history of wind-work on ocean inertial motions. *Geophys. Res. Lett.*, **30**, 1424, https://doi.org/10.1029/2002GL016614.

——, 2010: Sustained, full-water-column observations of internal waves and mixing near Mendocino escarpment. *J. Phys. Oceanogr.*, **40**, 2643–2660, https://doi.org/10.1175/2010JPO4502.1.

——, 2020a: Global calculations of local and remote near-inertial-wave dissipation. *J. Phys. Oceanogr.*, **50**, 3157–3164, https://doi.org/10.1175/JPO-D-20-0106.1.

——, 2020b: Revisiting near-inertial wind work: Slab models, relative stress, and mixed layer deepening. *J. Phys. Oceanogr.*, **50**, 3141–3156, https://doi.org/10.1175/JPO-D-20-0105.1.

——, and Z. Zhao, 2007a: Global patterns of low-mode internal-wave propagation. Part I: Energy and energy flux. *J. Phys. Oceanogr.*, **37**, 1829–1848, https://doi.org/10.1175/JPO3085.1.

——, and ——, 2007b: Global patterns of low-mode internal-wave propagation. Part II: Group velocity. *J. Phys. Oceanogr.*, **37**, 1849–1858, https://doi.org/10.1175/JPO3086.1.

——, M. F. Cronin, and J. M. Klymak, 2012: Annual cycle and depth penetration of wind-generated near-inertial internal waves at Ocean Station Papa in the northeast Pacific. *J. Phys. Oceanogr.*, **42**, 889–909, https://doi.org/10.1175/JPO-D-11-092.1.

Ansong, J. K., B. K. Arbic, M. C. Buijsman, J. G. Richman, J. F. Shriver, and A. J. Wallcraft, 2015: Indirect evidence for substantial damping of low-mode internal tides in the open ocean. *J. Geophys. Res. Oceans*, **120**, 6057–6071, https://doi.org/10.1002/2015JC010998.

——, and Coauthors, 2018: Geographical distribution of diurnal and semidiurnal parametric subharmonic instability in a global ocean circulation model. *J. Phys. Oceanogr.*, **48**, 1409–1431, https://doi.org/10.1175/JPO-D-17-0164.1.

Arbic, B. K., J. G. Richman, J. F. Shriver, P. G. Timko, E. J. Metzger, and A. J. Wallcraft, 2012: Global modeling of internal tides: Within an eddying ocean general circulation model. *Oceanography*, **25**, 20–29, https://doi.org/10.5670/oceanog.2012.38.

——, and Coauthors, 2018: Primer on global internal tide and internal gravity wave continuum modeling in HYCOM and MITgcm. *New Frontiers in Operational Oceanography*, GODAE OceanView, 307–392.

Asselin, O., and W. R. Young, 2020: Penetration of wind-generated near-inertial waves into a turbulent ocean. *J. Phys. Oceanogr.*, **50**, 1699–1716, https://doi.org/10.1175/JPO-D-15-0074.1.

Buijsman, M. C., and Coauthors, 2016: Impact of parameterized internal wave drag on the semidiurnal energy balance in a global ocean circulation model. *J. Phys. Oceanogr.*, **46**, 1399–1419, https://doi.org/10.1175/JPO-D-15-0074.1.

——, and Coauthors, 2020: On the interplay between horizontal resolution and wave drag and their effect on tidal baroclinic mode waves in realistic global ocean simulations. *Ocean Modell.*, **152**, 101656, https://doi.org/10.1016/j.ocemod.2020.101656.

Danioux, E., J. Vanneste, and O. Bühler, 2015: On the concentration of near-inertial waves in anticyclones. *J. Fluid Mech.*, **773**, R2, https://doi.org/10.1017/jfm.2015.252.

D'Asaro, E. A., C. C. Eriksen, M. D. Levine, C. A. Paulson, P. Niiler, and P. Van Meurs, 1995: Upper-ocean inertial currents forced by a strong storm. Part I: Data and comparisons with linear theory. *J. Phys. Oceanogr.*, **25**, 2909–2936, https://doi.org/10.1175/1520-0485(1995)025<2909:UOICFB>2.0.CO;2.

de Lavergne, C., S. Falahat, G. Madec, F. Roquet, J. Nycander, and C. Vic, 2019: Toward global maps of internal tide energy sinks. *Ocean Modell.*, **137**, 52–75, https://doi.org/10.1016/j.ocemod.2019.03.010.

Egbert, G. D., and R. D. Ray, 2001: Estimates of M_2 tidal energy dissipation from TOPEX/Poseidon altimeter data. *J. Geophys. Res.*, **106**, 22 475–22 502, https://doi.org/10.1029/2000JC000699.

Flexas, M. M., A. F. Thompson, H. S. Torres, P. Klein, J. T. Farrar, H. Zhang, and D. Menemenlis, 2019: Global estimates of the energy transfer from the wind to the ocean, with emphasis on near-inertial oscillations. *J. Geophys. Res. Oceans*, **124**, 5723–5746, https://doi.org/10.1029/2018JC014453.

Furuichi, N., T. Hibiya, and Y. Niwa, 2008: Model-predicted distribution of wind-induced internal wave energy in the world's oceans. *J. Geophys. Res.*, **113**, C09034, https://doi.org/10.1029/2008JC004768.

Gill, A., 1984: On the behavior of internal waves in the wakes of storms. *J. Phys. Oceanogr.*, **14**, 1129–1151, https://doi.org/10.1175/1520-0485(1984)014<1129:OTBOIW>2.0.CO;2.

Hallberg, R., 2005: A thermobaric instability of Lagrangian vertical coordinate ocean models. *Ocean Modell.*, **8**, 279–300, https://doi.org/10.1016/j.ocemod.2004.01.001.

Halliwell, G. R., 2004: Evaluation of vertical coordinate and vertical mixing algorithms in the hybrid-coordinate ocean model (HYCOM). *Ocean Modell.*, **7**, 285–322, https://doi.org/10.1016/j.ocemod.2003.10.002.

Hazewinkel, J., and K. Winters, 2011: PSI of the internal tide on a β plane: Flux divergence and near-inertial wave propagation. *J. Phys. Oceanogr.*, **41**, 1673–1682, https://doi.org/10.1175/2011JPO4605.1.

Hogan, T. F., and Coauthors, 2014: The Navy Global Environmental Model. *Oceanography*, **27**, 116–125, https://doi.org/10.5670/oceanog.2014.73.

Jiang, J., Y. Lu, and W. Perrie, 2005: Estimating the energy flux from the wind to ocean inertial motions: The sensitivity to surface wind fields. *Geophys. Res. Lett.*, **32**, L15610, https://doi.org/10.1029/2005GL023289.

Kang, D., and O. Fringer, 2010: On the calculation of available potential energy in internal wave fields. *J. Phys. Oceanogr.*, **40**, 2539–2545, https://doi.org/10.1175/2010JPO4497.1.

Kelly, S. M., 2016: The vertical mode decomposition of surface and internal tides in the presence of a free surface and arbitrary topography. *J. Phys. Oceanogr.*, **46**, 3777–3788, https://doi.org/10.1175/JPO-D-16-0131.1.

——, 2019: Coastally generated near-inertial waves. *J. Phys. Oceanogr.*, **49**, 2979–2995, https://doi.org/10.1175/JPO-D-18-0148.1.

Kunze, E., 1985: Near-inertial wave propagation in geostrophic shear. *J. Phys. Oceanogr.*, **15**, 544–565, https://doi.org/10.1175/1520-0485(1985)015<0544:NIWPIG>2.0.CO;2.

——, 2017: Internal-wave-driven mixing: Global geography and budgets. *J. Phys. Oceanogr.*, **47**, 1325–1345, https://doi.org/10.1175/JPO-D-16-0141.1.

Le Boyer, A., and M. H. Alford, 2021: Variability and sources of the internal wave continuum examined from global moored velocity records. *J. Phys. Oceanogr.*, **51**, 2807–2823, https://doi.org/10.1175/JPO-D-20-0155.1.

Lee, D.-K., and P. P. Niiler, 1998: The inertial chimney: The near-inertial energy drainage from the ocean surface to the deep layer. *J. Geophys. Res.*, **103**, 7579–7591, https://doi.org/10.1029/97JC03200.

Liang, C.-R., G.-Y. Chen, X.-D. Shang, X.-H. Xie, and D.-X. Wang, 2019: Observation of enhanced nonlinear interactions after severe Tropical Storm Chanchu (2004) in the western South China Sea. *J. Geophys. Res. Oceans*, **124**, 3837–3848, https://doi.org/10.1029/2018JC014839.

MacKinnon, J. A., and Coauthors, 2017: Climate process team on internal wave–driven ocean mixing. *Bull. Amer. Meteor. Soc.*, **98**, 2429–2454, https://doi.org/10.1175/BAMS-D-16-0030.1.

Metzger, E. J., and Coauthors, 2014: US Navy operational global ocean and Arctic ice prediction systems. *Oceanography*, **27**, 32–43, https://doi.org/10.5670/oceanog.2014.66.

Mishra, K., M. Sharma, and M. Mohapatra, 2021: Performance of numerical weather prediction models in predicting track of recurving Cyclone Vayu over Arabian Sea during June 2019. *J. Earth Syst. Sci.*, **130**, 25, https://doi.org/10.1007/s12040-020-01533-7.

Mooers, C. N., 1975: Several effects of a baroclinic current on the cross-stream propagation of inertial-internal waves. *Geophys. Astrophys. Fluid Dyn.*, **6**, 245–275, https://doi.org/10.1080/03091927509365797.

Morvan, M., X. Carton, S. Corréard, and R. Baraille, 2020: Submesoscale dynamics in the Gulf of Aden and the Gulf of Oman. *Fluids*, **5**, 146, https://doi.org/10.3390/fluids5030146.

Müller, M., B. K. Arbic, J. G. Richman, J. F. Shriver, E. L. Kunze, R. B. Scott, A. J. Wallcraft, and L. Zamudio, 2015: Toward an internal gravity wave spectrum in global ocean models. *Geophys. Res. Lett.*, **42**, 3474–3481, https://doi.org/10.1002/2015GL063365.

Munk, W., and C. Wunsch, 1998: Abyssal recipes II: Energetics of tidal and wind mixing. *Deep-Sea Res. I*, **45**, 1977–2010, https://doi.org/10.1016/S0967-0637(98)00070-3.

Nash, J. D., M. H. Alford, and E. Kunze, 2005: Estimating internal wave energy fluxes in the ocean. *J. Atmos. Oceanic Technol.*, **22**, 1551–1570, https://doi.org/10.1175/JTECH1784.1.

Nikurashin, M., and R. Ferrari, 2011: Global energy conversion rate from geostrophic flows into internal lee waves in the deep ocean. *Geophys. Res. Lett.*, **38**, L08610, https://doi.org/10.1029/2011GL046576.

Plueddemann, A., and J. Farrar, 2006: Observations and models of the energy flux from the wind to mixed-layer inertial currents. *Deep-Sea Res. II*, **53**, 5–30, https://doi.org/10.1016/j.dsr2.2005.10.017.

Pollard, R. T., and R. Millard Jr., 1970: Comparison between observed and simulated wind-generated inertial oscillations. *Deep-Sea Res. Oceanogr. Abstr.*, **17**, 813–821, https://doi.org/10.1016/0011-7471(70)90043-4.

Polzin, K. L., and Y. V. Lvov, 2011: Toward regional characterizations of the oceanic internal wavefield. *Rev. Geophys.*, **49**, RG4003, https://doi.org/10.1029/2010RG000329.

Rainville, L., and R. Pinkel, 2006: Propagation of low-mode internal waves through the ocean. *J. Phys. Oceanogr.*, **36**, 1220–1236, https://doi.org/10.1175/JPO2889.1.

Rimac, A., 2014: The role of wind induced near-inertial waves on the energetics of the ocean. Ph.D. thesis, Universität Hamburg, 117 pp., https://pure.mpg.de/rest/items/item_2075939_5/component/file_2075949/content.

——, J.-S. von Storch, C. Eden, and H. Haak, 2013: The influence of high-resolution wind stress field on the power input to near-inertial motions in the ocean. *Geophys. Res. Lett.*, **40**, 4882–4886, https://doi.org/10.1002/grl.50929.

——, ——, and ——, 2016: The total energy flux leaving the ocean's mixed layer. *J. Phys. Oceanogr.*, **46**, 1885–1900, https://doi.org/10.1175/JPO-D-15-0115.1.

Sanford, T. B., B. B. Ma, and M. H. Alford, 2021: Stalling and dissipation of a near-inertial wave (NIW) in an anticyclonic ocean eddy: Direct determination of group velocity and comparison with theory. *J. Geophys. Res. Oceans*, **126**, e2020JC016742, https://doi.org/10.1029/2020JC016742.

Scott, R., J. Goff, A. Naveira Garabato, and A. Nurser, 2011: Global rate and spectral characteristics of internal gravity wave generation by geostrophic flow over topography. *J. Geophys. Res.*, **116**, C09029, https://doi.org/10.1029/2011JC007005.

Shakespeare, C. J., 2020: Interdependence of internal tide and lee wave generation at abyssal hills: Global calculations. *J. Phys. Oceanogr.*, **50**, 655–677, https://doi.org/10.1175/JPO-D-19-0179.1.

Simmons, H. L., and M. H. Alford, 2012: Simulating the long-range swell of internal waves generated by ocean storms. *Oceanography*, **25**, 30–41, https://doi.org/10.5670/oceanog.2012.39.

Singh, A. K., and B. Bhadauria, 2009: Finite difference formulae for unequal sub-intervals using Lagrange's interpolation formula. *Int. J. Math. Anal.*, **3**, 815–827.

Thomas, L. N., L. Rainville, O. Asselin, W. R. Young, J. Girton, C. B. Whalen, L. Centurioni, and V. Hormann, 2020: Direct observations of near-inertial wave ζ-refraction in a dipole vortex. *Geophys. Res. Lett.*, **47**, e2020GL090375, https://doi.org/10.1029/2020GL090375.

Trossman, D. S., B. K. Arbic, S. T. Garner, J. A. Goff, S. R. Jayne, E. J. Metzger, and A. J. Wallcraft, 2013: Impact of parameterized lee wave drag on the energy budget of an eddying global ocean model. *Ocean Modell.*, **72**, 119–142, https://doi.org/10.1016/j.ocemod.2013.08.006.

Van Haren, H., 2005: Tidal and near-inertial peak variations around the diurnal critical latitude. *Geophys. Res. Lett.*, **32**, L23611, https://doi.org/10.1029/2005GL024160.

Vic, C., and Coauthors, 2019: Deep-ocean mixing driven by small-scale internal tides. *Nat. Commun.*, **10**, 2099, https://doi.org/10.1038/s41467-019-10149-5.

Watanabe, M., and T. Hibiya, 2002: Global estimates of the wind-induced energy flux to inertial motions in the surface mixed layer. *Geophys. Res. Lett.*, **29**, 1239, https://doi.org/10.1029/2001GL014422.

Whalen, C. B., J. A. MacKinnon, and L. D. Talley, 2018: Large-scale impacts of the mesoscale environment on mixing from wind-driven internal waves. *Nat. Geosci.*, **11**, 842–847, https://doi.org/10.1038/s41561-018-0213-6.

Xie, X.-H., X.-D. Shang, H. van Haren, G.-Y. Chen, and Y.-Z. Zhang, 2011: Observations of parametric subharmonic instability-induced near-inertial waves equatorward of the critical diurnal latitude. *Geophys. Res. Lett.*, **38**, L05603, https://doi.org/10.1029/2010GL046521.

Young, W., and M. B. Jelloul, 1997: Propagation of near-inertial oscillations through a geostrophic flow. *J. Mar. Res.*, **55**, 735–766, https://doi.org/10.1357/0022240973224283.

Zaron, E. D., and G. D. Egbert, 2014: Time-variable refraction of the internal tide at the Hawaiian ridge. *J. Phys. Oceanogr.*, **44**, 538–557, https://doi.org/10.1175/JPO-D-12-0238.1.

Zhai, X., R. J. Greatbatch, C. Eden, and T. Hibiya, 2009: On the loss of wind-induced near-inertial energy to turbulent mixing in the upper ocean. *J. Phys. Oceanogr.*, **39**, 3040–3045, https://doi.org/10.1175/2009JPO4259.1.